Astronomy & Astrophysics manuscript no. main
December 28, 2021

Magnetic field amplification and structure formation by the Rayleigh-Taylor instability.

B. Popescu Braileanu[1, 2, 3] *, V. S. Lukin[4], and E. Khomenko[2, 3]

[1] Centre for mathematical Plasma Astrophysics, KU Leuven, 3001, Leuven, Belgium
[2] Instituto de Astrofísica de Canarias, 38205 La Laguna, Tenerife, Spain
[3] Departamento de Astrofísica, Universidad de La Laguna, 38205, La Laguna, Tenerife, Spain
[4] National Science Foundation, Alexandria, VA, 22306, USA

Received 2021; Accepted XXXX

ABSTRACT

We report on results of high resolution two fluid non-linear simulations of the Rayleigh Taylor Instability (RTI) at the interface between a solar prominence and the corona. These follow results reported earlier by Popescu Braileanu et al. (2021a,b) on linear and early non-linear RTI dynamics in this environment. The simulations use a two fluid model that includes collisions between neutrals and charges, including ionization/recombination, energy and momentum transfer, and frictional heating. High resolution 2.5D magnetized RTI simulations with the magnetic field dominantly normal to and slightly sheared with respect to the prominence plane demonstrate that in a fully developed state of RTI a large fraction of the gravitational energy of a prominence thread can be converted into quasi-turbulent energy of the magnetic field. RTI magnetic energy generation is further accompanied by magnetic and plasma density structure formation, including dynamic formation, break-up, and merging of current sheets and plasmoid sub-structures. The simulations show the role of flow decoupling and ionization/recombination reactions between the neutrals and charges on the structure formation in magnetized RTI. We provide a careful examination of sources and form of numerical dissipation of the evolving magnetic field structures.

Key words. Sun: chromosphere – Sun: magnetic field – Sun: numerical simulations – Sun: magnetic reconnection

1. Introduction.

Rayleigh Taylor Instability (RTI) is an instability which occurs in many astrophysical contexts when a heavier fluid is accelerated against a lighter one. In the Sun, RTI is routinely detected in high-resolution observations of solar prominences. This instability manifests itself as small scale upflows and downflows at the interface between prominences and the corona (Berger et al. 2017; Hillier & Polito 2018). Several numerical models of the magnetic RTI for solar conditions have been reported in the literature (see e.g., Hillier et al. 2012b,a; Keppens et al. 2015; Terradas et al. 2016). These models, done under under MHD approximation, allowed to access the non-linear stages of the instability and study the plasma mixing, reconnection and the associated dynamical events.

Solar prominences are composed of chromospheric material, which is much denser and cooler than the surrounding corona (Labrosse et al. 2010). The prominences are partially ionized with the collisional timescale between neutrals and charges comparable to the hydrodynamic timescale. Therefore, MHD modeling of prominence RTI is not enough to describe the physics at small scales and multi-fluid models of RTI are required. In our recent work (Popescu Braileanu et al. 2021a,b) we have modeled RTI in the two-fluid approximation in a configuration proposed initially by Leake et al. (2012). These simulations have demonstrated how the RTI cut-off can be affected by ion-neutral effects, and have shown the complex non-linear dynamical phenomena with decoupling between the charged and neutral components. The aim of the current paper is to study in detail the dynamics and the structure formation associated with non-linear RTI development.

In a purely hydrodynamic RTI with a discontinuous interface, the linear theory shows that all RTI modes are unstable (Chandrasekhar 1961). The same also holds for a magnetized plasma when the magnetic field is perpendicular to the perturbation plane. However, a component of the magnetic field parallel to the direction of the perturbation inhibits the growth of the small-scale modes (Chandrasekhar 1961). Interestingly, when the magnetic field is sheared with respect to the perturbation plane, the linear theory shows the absence of a cutoff in the ideal MHD case (Popescu Braileanu et al. 2021a,b).

During the non-linear phases of the instability, the mixing becomes turbulent. When there is a magnetic field component parallel to the direction of the perturbation, the in-plane magnetic field lines are stretched

---

* e-mail: `beatriceannemone.popescubraileanu@kuleuven.be`

and the field is amplified (Jun et al. 1995; Zhou et al. 2021). The magnetic field lines brought together by the flow create current sheets, which can reconnect. The current sheets can become unstable creating secondary magnetic structures called plasmoids.

There have been a number of studies where magnetic reconnection was investigated using a two-fluid ion-neutral model under controlled and idealized setups. It has been demonstrated that, when ions and neutrals are allowed to have independent dynamics, they can collisionally decouple in inflows, but are still coupled in outflows (Leake et al. 2012). Two-fluid effects have been shown to increase the reconnection rates compared to a classical Sweet-Parker model (Leake et al. 2012; Ni et al. 2018b) in some collisionality regimes. The Hall effect, and the formation of plasmoids in the current sheet also enhance the reconnection rates (Ni et al. 2018b; Ni & Lukin 2018), while radiative losses do not influence qualitatively the reconnection process (Ni & Lukin 2018). Here we study a different situation where the reconnecting current sheet is naturally created by the dynamics associated with RTI.

We describe a high resolution simulation of RTI in a 2.5D geometry with parameters corresponding to a solar prominence thread and in a setup described as L1-WN in Table 1 in Popescu Braileanu et al. (2021a). The numerical box of the size 2 × 8 Mm is covered by 2048 × 8192 grid points, which is 4 times higher resolution than in our previous work. The magnetic field of approximate strength of 10 G is directed out of the perturbation plane, inclined by 1 degree and sheared over 1 Mm scale. There is a smooth transition between the prominence thread and the corona.

We describe the overall dynamics of the RTI, and the magnetic field amplification in Section 2. We analyze formation of reconnection current sheets, secondary plasmoid instabilities, and the resulting spectra of magnetic and plasma density structures in Section 3. We present our conclusions in Section 4.

2. Magnetized RTI dynamics and magnetic field amplification.

Non-linear development of RTI leads to formation of downflows (spikes) and upflows (bubbles). These structures can be seen in Figure 1, which illustrates the evolution of the instability over the fully developed phase. The mass density of the charges (top row) and the mass density of the neutrals (bottom row) show similar isodensity contours, with regions of high neutral density corresponding to regions of low density of charges. As bubbles and spikes form, the in-plane magnetic field lines are dragged and stretched by the motion of the plasma. This is shown in the top panels of Figure 1, where the magnetic field lines are plotted over the colormap of density of the charges. We observe the field lines to follow the isodensity contours, and observe a significant increase in the magnitude of the in-plane field, illustrated as the density of field lines, enveloping the spikes and upflows over time. Around time 534.5 sec (middle panels) one can observe that two bigger drops are brought together by the flow and start merging. This merging results in formation of one single spike, visible in the last two panels, which has complex internal structure. In particular, one can observe formation of current sheets and plasmoids. One of the bigger plasmoids is clearly visible at the last panel as a dark/bright circular structure in the charged(top)/neutral(bottom) density images. It is filled with the hotter and more ionized coronal-like material.

The generation of in-plane magnetic energy by the RTI is quantified in Figure 2. The left hand side panel of Figure 2 shows the horizontal average of the out-of-plane magnetic energy (solid lines, left axis) and in-plane magnetic energy (dotted lines, right axis) as a function of height for the same time moments as shown in Figure 1. The right hand side panel shows the time evolution of the out-of-plane magnetic energy, the in-plane magnetic energy, as well as the kinetic energies of charges and neutrals averaged over the full domain. We observe that the amount of in-plane magnetic energy rapidly grows as RTI develops, with concentrations of energy immediately above and below the bubbles and spikes. There is a small decrease in the amount of out-of-plane magnetic energy, but it does not appear to be dynamically significant. We note that the initial free energy is mostly in the gravitational energy of the prominence thread, with high neutral density supported by a small increase in magnetic field strength at the prominence-corona interface. The right hand side panel of Figure 1 demonstrates that most of the free energy goes into the generation of the in-plane magnetic field. While we observe an initial increase in the kinetic energy of neutrals, and to a smaller extent charges, as the bubbles and spikes accelerate, the in-plane magnetic field appears to contain and absorb plasma flows. At the conclusion of the simulation, we observe the increase in magnetic energy (solid green line) to be approximately twice the total increase in the kinetic energy of neutrals (solid violet line) and charges (solid orange line).

To verify our conclusions and estimate the amount of numerical dissipation impacting magnetic field generation, we also calculate the work done by RTI flows against both the in-plane and out-of-plane components of the Lorentz force, as shown in the right panel of Figure 2. For both components, we observe that the corresponding magnetic energy curve shows slightly smaller values, the difference being due to the numerical magnetic diffusivity, as discussed below and quantified in Appendix A.

3. Formation of current sheets, magnetic and plasma structures.

At large scales the magnetic field is frozen in the plasma and the mixing brings field lines with different orientation close, thus creating current sheets. At small scales, magnetic diffusivity acts to reconnect the field lines.

We recall that the simulations described here and in (Popescu Braileanu et al. 2021a,b) do not include an explicit resistivity term in the Ohm's Law and the magnetic diffusivity is numerical. The functional form

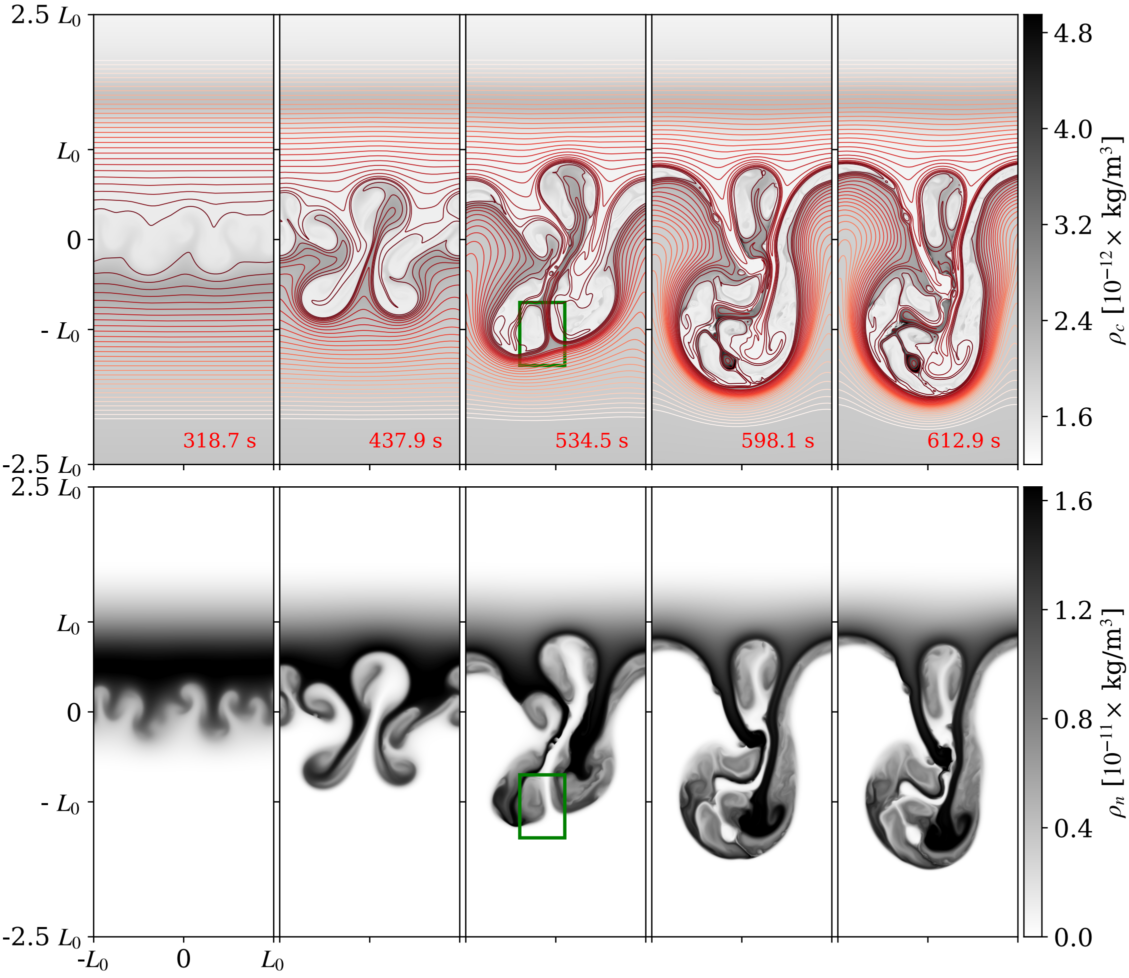

Fig. 1. Snapshots of the non-linear evolution of the RTI at $t = [318.7\ s, 437.9\ s, 534.5\ s, 598.1\ s, 612.9\ s]$ for $(x, z) \in [-L_0, L_0] \times [-2.5\ L_0, 2.5\ L_0]$. The top panels illustrate the evolution of the in-plane projection of the magnetic field lines overlaid on a grayscale colormap of the mass density of the charges. The bottom panels similarly show the spatial distribution and dynamical evolution of the mass density of the neutrals. The rectangular box marked in the $t = 534.5\ s$ panels corresponds to the zoom-in views of a reconnecting current sheet shown in Figs. 3-4 below.

of the numerical diffusivity and the value of the corresponding coefficient in the present MANCHA3D-2F implementation are described in Appendix A. In particular, we estimate that numerical magnetic diffusivity within observed current sheets for the simulation described in this paper is more than an order of magnitude greater than the physical diffusivity due to Spitzer resistivity would be. Thus, given the practical limitations of a numerical simulation, we are justified in omitting the resistivity term from the Ohm's Law.

Figure 3 shows the evolution of charged fluid density in the window drawn in the middle panels of Figure 1, which captures the two merging spikes. The current density contours are overplotted and we observe formation of current sheets associated with diffusion of the magnetic field. As the system evolves, the current sheets repeatedly elongate and break up, leading to the formation of smaller secondary magnetic structures. The series of snapshots in Fig. 3 documents at least five such instances, with the resulting small plasmoids themselves merging and several joining into a larger one seen at the bottom of the window. The critical length-to-width ratio of the current sheets before they break up consistently appears to be ≈ 20. We also observe that the merging plasmoids lead to formation of not only magnetic but also density structures, with the electron density in the large resulting plasmoid significantly exceeding the ambient coronal electron density prior to RTI development.

As the spikes filled with largely neutral material attempt to merge, the Lorentz force slows down the charged particles across the field lines while the neu-

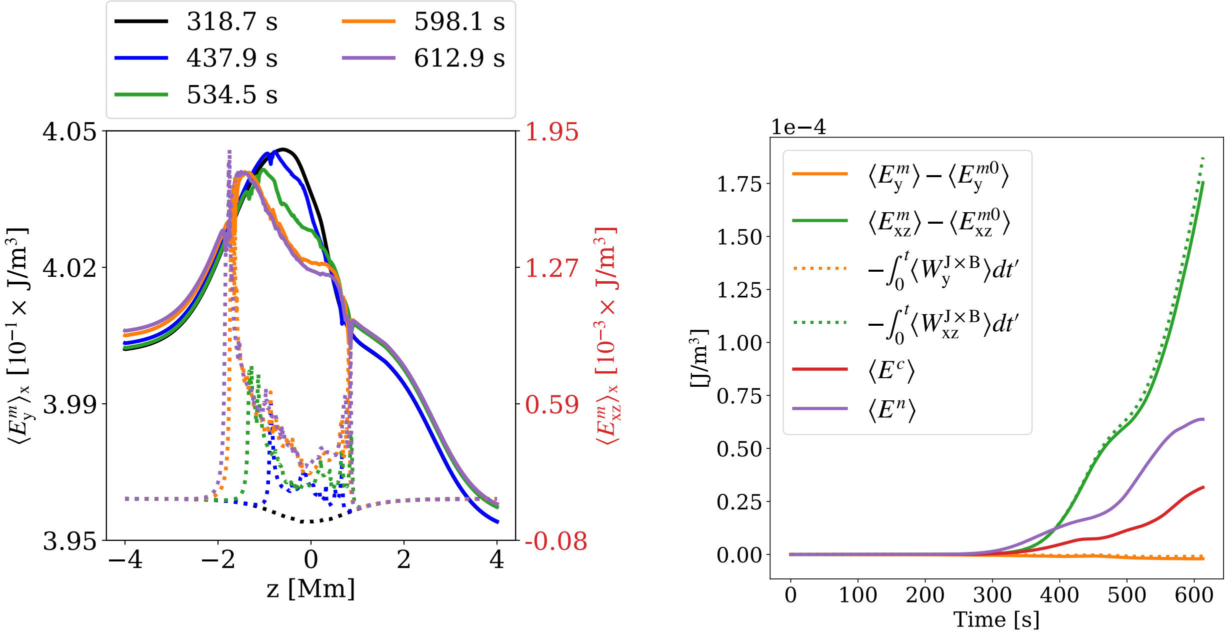

Fig. 2. Left: Magnetic energy in out-of-plane component of the magnetic field, $\langle E^m_{\rm y}\rangle_{\rm x}$ (solid lines, values on the left axis) and the in-plane magnetic energy $\langle E^m_{\rm xz}\rangle_{\rm x}$ (dotted lines, values on the right axis), as a function of height and averaged in x, plotted at the times corresponding to the panels in Fig. 1. Right: Spatially averaged components of energy density in the computational domain as a function of time. $\langle E^m_{\rm y}\rangle - \langle E^{m0}_{\rm y}\rangle$ denotes the change in the magnetic energy density due to evolution of out-of-plane component of magnetic field B_y; $\langle E^m_{\rm xz}\rangle - \langle E^{m0}_{\rm xz}\rangle$ denotes the change in the magnetic energy density due to evolution of in-plane components of magnetic field B_x and B_z; $-\int_0^t \langle W^{J\times B}_{\rm y}\rangle dt'$ and $-\int_0^t \langle W^{J\times B}_{\rm xz}\rangle dt'$ denote work done by the RTI against the $\mathbf{F} = \mathbf{J}\times\mathbf{B}$ force up to time t in evolving the out-of-plane and in-plane magnetic field components, respectively. $W^{J\times B} = \mathbf{F}\cdot\mathbf{v_c} = W^{J\times B}_{\rm xz} + W^{J\times B}_{\rm y}$, with $W^{J\times B}_{\rm xz} = J_y\left(B_z v_{cx} - B_x v_{cz}\right)$ and $W^{J\times B}_{\rm y} = B_y\left(J_x v_{cz} - J_z v_{cx}\right)$. E^c is the kinetic energy density of the charges; and E^n is the kinetic energy density of the neutrals.

trals are not affected by the magnetic field. The decoupling in velocity between charges and neutrals is shown in Fig. 3 by orange arrows and appears largest around the edges of the spikes and across the current sheet.

In order to study a reconnecting current sheet in more detail, we choose a moment of time when a single current sheet is clearly defined. Figure 4 shows the charged fluid density at time t=534.5 s, which is the same moment of time as for the second snapshot in the sequence shown in Figure 3. The in-plane magnetic field lines and the arrows showing the charged fluid velocity are overplotted, noting that the larger scale structures are moving downwards and to the left. We then project different quantities along the dashed red line drawn in Figure 4, which was calculated to be the direction perpendicular to the current sheet. These 1D profiles across the current sheet are shown in Figure 5.

The 1D profiles capture the outer inflow region of the reconnection current sheet, showing the two spikes consisting mainly of neutral material approaching each other. This is reflected in panel (a) of Fig. 5, with the neutral density shown with the dashed line being larger outside the current sheet, but diminishing within the current sheet with the plasma becoming close to fully ionized. The edges of the spikes become ionized while moving into the much hotter corona and this fact is reflected in the two small peaks in the charged density outside the current sheet, shown with the solid line in panel (a).

Panel (b) of Fig. 5 shows that plasma is flowing into the current from both left and right, while the overall motion of the spikes noted above leads to the drift of the whole current sheet system. The decoupling in velocities, shown with the dashed line in panel (b), is significant at more than 20% of the inflow velocity. We note that the symmetric nature of the decoupling centered at the current sheet confirms that the decoupling is indeed associated with the reconnection process. The neutrals which are dominant in the spikes are flowing into the current sheet faster, making the decoupling velocity between charges and neutrals point outwards in the current sheet.

The reversal of the reconnecting component of the magnetic field is illustrated in panel (c) and the magnitude of the reconnection current, J_y, in panel (d) of Fig. 5. We note that the reconnecting field of ≈ 0.5 G is 5% of the out-of-plane "guide" magnetic field shown in panel (e). We also note that the guide field peaks at the center of the reconnection current sheet. An estimate of the variation in the reconnecting and guide field components of the magnetic field from panels (c) and (e) shows that the magnitude of magnetic field strength is approximately constant across the current

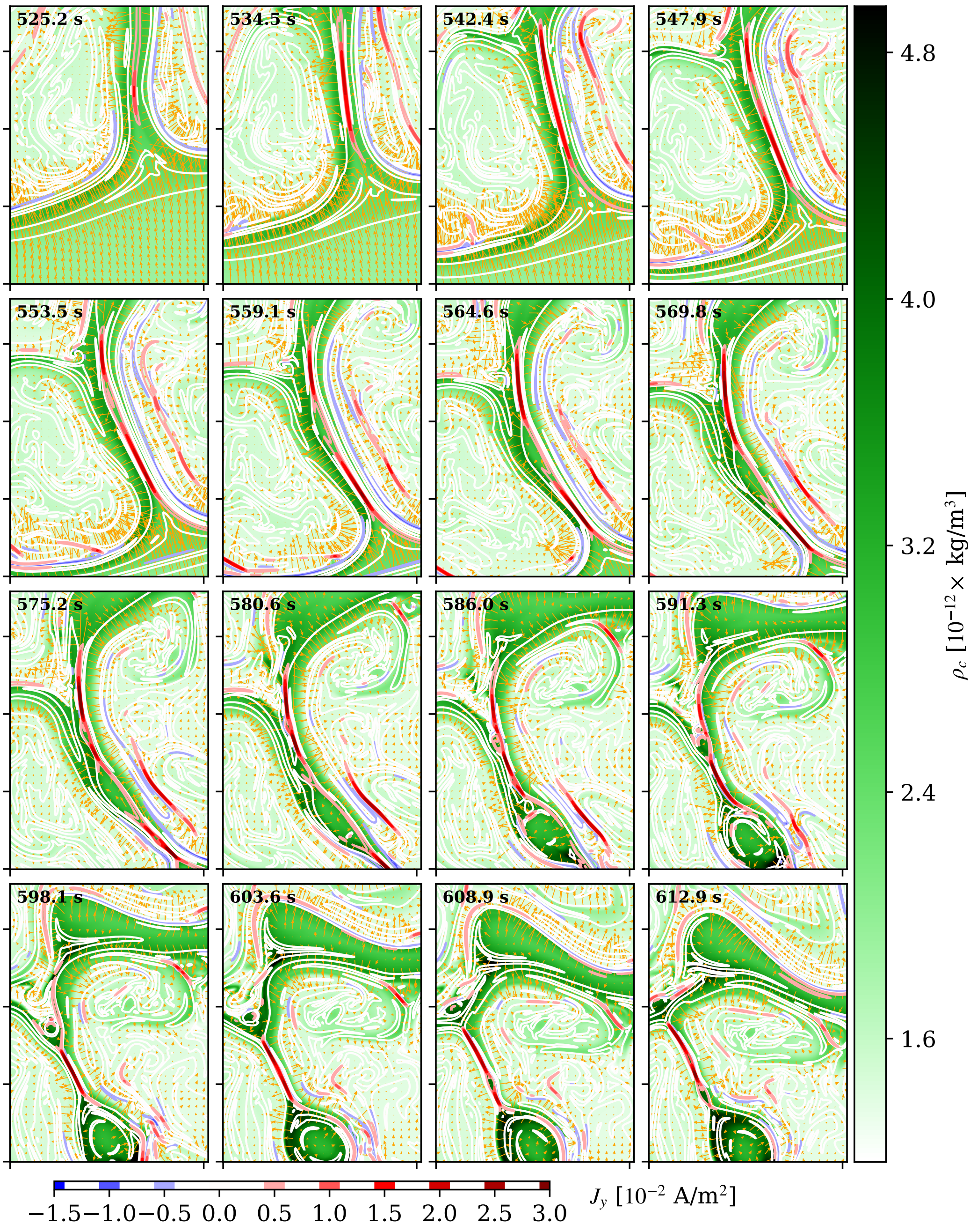

Fig. 3. A snapshot sequence of dynamic evolution of a reconnecting current layer with recurring plasmoid formation is shown with color contours of the out-of-plane current density J_y and arrows showing difference in the in-plane flow between charges and neutrals $(\mathbf{v}_c - \mathbf{v}_n)_{xz}$ plotted over a colormap of the mass density of charges. The snapshot window is illustrated in the $t = 534.5$ s panels of Fig. 1 and has coordinates $(x, z) \in [-0.4 \text{ Mm}, 0.1 \text{ Mm}] \times [-1.4 \text{ Mm}, -0.7 \text{ Mm}]$. An arrow with length of 50 km corresponds to a speed difference of $|(\mathbf{v}_c - \mathbf{v}_n)_{xz}| = 128$ m/s.

sheet. Thus, while the in-plane and out-of-plane magnetic field components both have spatial structure on the current sheet scales, the magnitude of B-field appears to have less structure on the smallest scales.

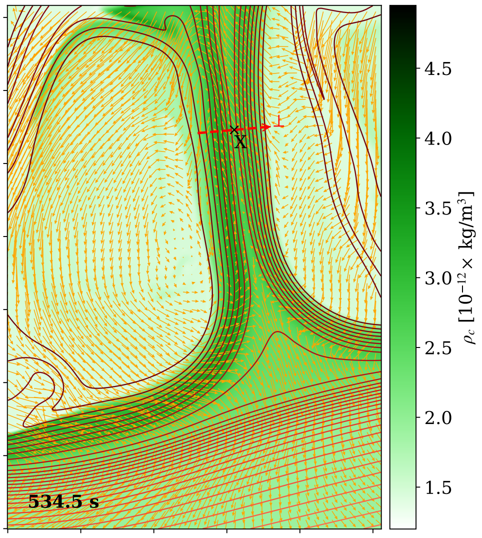

Fig. 4. Snapshot of a reconnecting current sheet at $t = 534.5\ s$ with contours denoting in-plane projection of magnetic field lines, arrows showing the relative magnitude and direction of the in-plane flow of the charged fluid $\mathbf{v}_c$, and a colormap of the density of the mass density of charges ρ_c. The snapshot window is the same as in Fig. 3 above. An arrow with length of 50 km corresponds to a speed of $|(\mathbf{v}_c)_{xz}| = 12.8$ km/s. The center x-point of the current sheet determined as the location of the maximum out-of-plane current density J_y is marked with 'X' in the image and is located at $(x, z) = (-0.097\ \text{Mm}, -0.867\ \text{Mm})$. The dashed red line marks a cut across the current sheet in the direction perpendicular to the reconnecting magnetic field lines.

Panel (f) of Fig. 5 shows contributions to the out-of-plane component of the electric field in the frame of reference of the moving current sheet: the ideal contribution (solid black line) that drives the reconnection process, and the non-ideal contribution (dashed green line) due to the numerical diffusion estimated in Appendix A that represents the resulting reconnection rate. We note that the total E_y-field, the sum of the two contributions, has a minimum at the center of the current sheet, which is typical for driven magnetic reconnection (Birn & Hesse 2007).

The spatial correlation between the in-plane and out-of-plane magnetic structures can also be observed in the spectra of component contributions to magnetic energy shown for the latest time of the simulation in the left panel of Figure 6. At intermediate and small scales, the content of magnetic energy is very similar for the in-plane and out-of-plane components, with much less content in the total magnetic energy. This is consistent with the magnetic field profiles across the current sheet shown in Figure 5 and the conclusion reached in (Popescu Braileanu et al. 2021a) for small scale magnetic structures.

The left panel of Figure 6 also shows the structure spectrum for mass density of the charged fluid. A linear fit in the intermediate scale range is done for the spectra of the total magnetic energy (blue) and the charged fluid density (light green), showing that the two are distinct within the standard deviation of the fit procedure described in the figure caption. The right panel of Figure 6 demonstrates that towards the end of the simulation the slopes of both spectra evolve to a stationary value, indicating that the simulation appears to have reached a fully developed non-linear RTI state.

4. Conclusions.

The results described above demonstrate that fully developed RTI in a weakly sheared magnetic field background can act to transfer the bulk of the released gravitational energy into amplification of magnetic field with associated magnetic and plasma structure formation on multiple scales. The mixing between neutral and ionized fluids leads to stretching of magnetic field lines around RTI fingers that begin to interact via current sheets. The current sheets, in turn, become unstable to secondary instabilities that lead to further magnetic and plasma structure formation, including generation and merging of magnetic flux ropes, enhanced plasma heating, and formation of highly ionized plasma structures with electron density significantly above ambient corona electron density.

As described in Popescu Braileanu et al. (2021a,b), the linear and early non-linear evolution of magnetized RTI in a sheared magnetic field can strongly depend on the shear scale relative to the density gradient scale driving the RTI. In this paper, we focused on a prominence thread configuration with the same magnetic shear and density gradient scales. This configuration allows simultaneous growth and development of several RT modes, which leads to robust mixing between the high density and dominantly neutral prominence material and the low density, magnetized, and well-ionized coronal plasma. At the same time, due to the stabilizing presence of the sheared magnetic field, there is limited plasma mixing on short spatial scales, and the potential gravitational energy initially stored in the high density neutral material is largely deposited into the magnetic field energy by stretching the magnetic field lines on intermediate spatial scales.

The interaction between magnetic field structures resulting from the early non-linear RTI development inevitably leads to formation of current sheets and associated dissipation of the magnetic energy. While the set of two-fluid MHD equations evolved in this study does not include explicit dissipation terms in the Ohm's Law, we demonstrate that the 6th order spatial filtering procedure applied during the temporal advance of the PDEs in the Mancha3D-2F code is the primary source of the dissipation of the magnetic field in current sheets.

Magnetic reconnection between RTI-generated magnetic structures observed in the simulation is driven by the convective flows of the RTI fingers and the neutral fluid pressure gradient at their edges. It is driven two-fluid magnetic reconnection with strong guide field, with neutral flows pushing the magnetic fields with oppositely directed in-plane components towards each other and producing flow decoupling be-

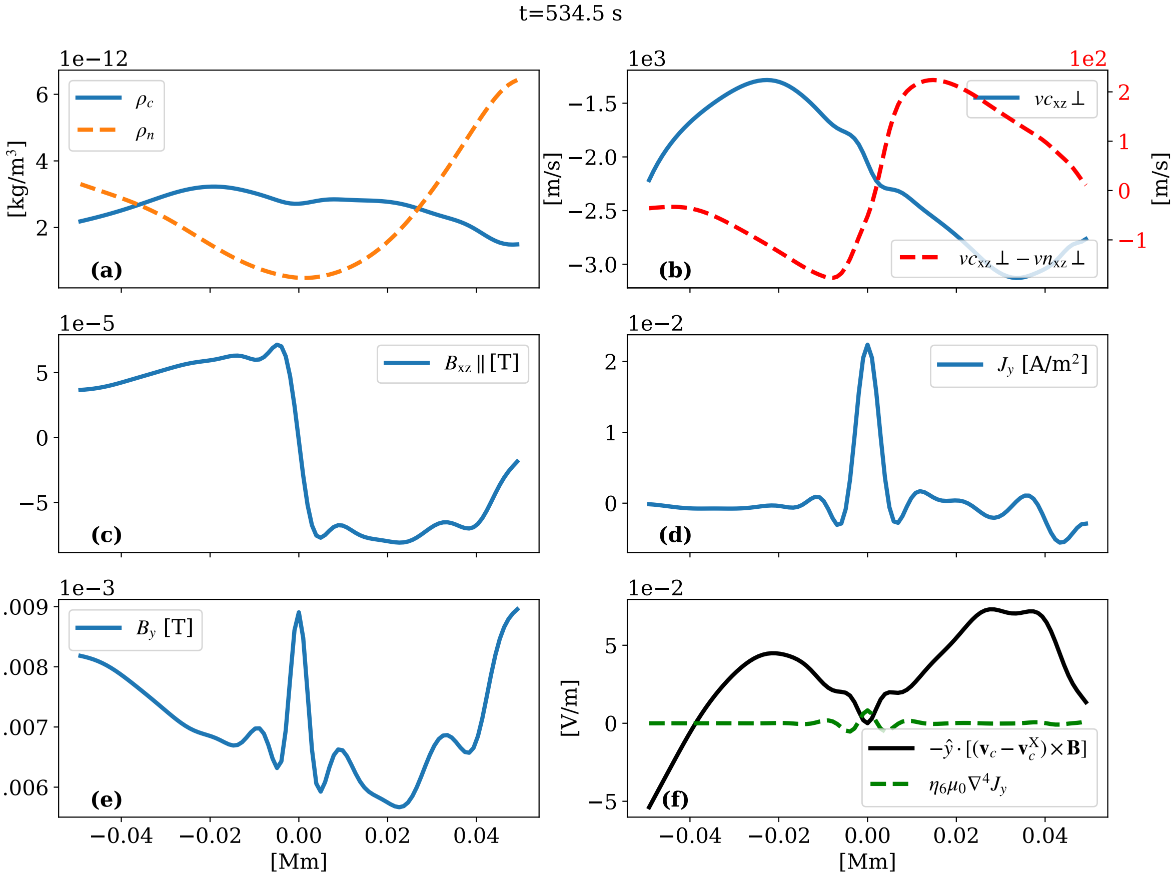

Fig. 5. Profiles across a reconnecting current sheet at $t = 534.5$ s along the cut marked with the dashed red line in Fig. 4 and centered with the 0 location along the cut to correspond to the X-point location in Fig. 4. The panels show (a) mass density of neutrals (dashed orange line) and charges (solid blue line); (b) the flow velocity along the direction of the cut for the charges (solid blue line) as well as the relative drift between charges and neutrals (dashed red line); (c) the in-plane magnetic field component normal to the cut and along the current sheet; (d) the out-of-plane current density J_y; and (e) the out-of-plane magnetic field B_y. Panel (f) shows the calculated ideal electric field $E_y = -\hat{y}\cdot[(\mathbf{v}_c - \mathbf{v}_c^X)\times\mathbf{B}]$ in the frame of reference of the charged fluid at the X-point (solid black line), and the $\hat{y}$-component of the effective dissipative electric field, $\eta_6\mu_0\nabla^4 J_y$, present due to numerical dissipation (dashed green line). The width of the reconnection current sheet is measured to be $\lambda_J = 5.323$ km as the full width at half max of the J_y profile in panel (f).

tween the neutral and charged inflows at $\approx 20\%$ of the neutral inflow speed. Concurrent ionization of the inflowing neutral prominence material due to higher ambient temperature of the plasma between RTI fingers, as well as dissipative heating, results in current sheets being embedded within plasma structures with high ionization fraction and electron density.

Unlike prior work on two-fluid guide field reconnection in a weakly ionized plasma by Ni et al. (2018a,b), here the ionization and recombination processes do not play a dynamical role in determining the sub-structure of the reconnection current sheet. This is due to several factors, including the ambient plasma parameters with lower ionization and recombination rates relative to the current sheet formation time, and the driven rather than spontaneous nature of the reconnection process. It is also important to note that the present model does not include optically thin radiative losses included in the two-fluid model used by Ni et al. (2018a) and Ni et al. (2018b), which was shown in Ni et al. (2018b) to strongly impact the temperature and density current sheet sub-structure in some plasma regimes.

The driven reconnection process results in recurring formation of small scale magnetic flux ropes within the current sheet, often referred to in the literature as plasmoids, when the current sheet length-to-width aspect ratio approaches ≈ 20, a value that is a factor of several lower than that reported by Ni & Lukin (2018). While the numerical nature of the dissipation in the present simulation makes it difficult to generalize this result to other driven reconnection systems, this appears to be a robust feature of the current system as demonstrated in Fig. 3. Further dedicated effort to explore stability of driven current sheets in a partially ionized plasma would be necessary to make more definitive conclusions regarding specific current sheet aspect ratio stability thresholds.

The RTI-driven plasma and magnetic field mixing, formation of current sheets within well-ionized plasma layers between RTI fingers, and the recurring formation of secondary magnetic and plasma substructures naturally leads to the development of a spectrum of structures at different scales. We demonstrate that fully developed magnetized RTI can lead to emergence

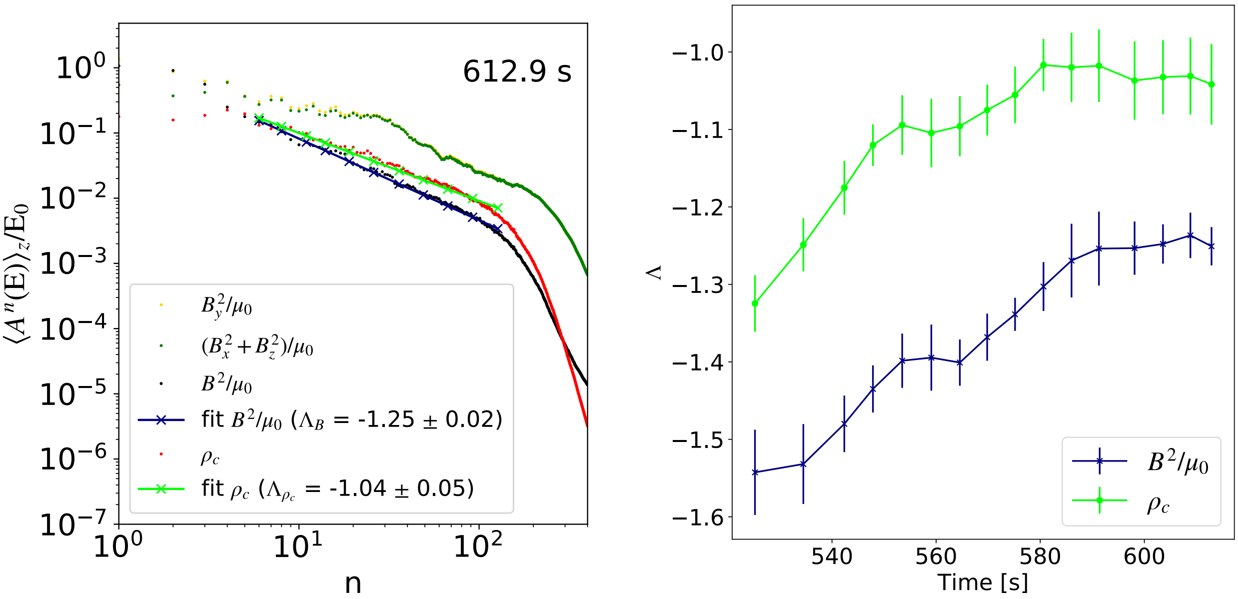

Fig. 6. Left: Fourier decomposition of spatial structure in magnetic field and mass density of charges in the periodic x-direction at $t = 612.9$ s. For each horizontal mode n, amplitudes are calculated and averaged in height over the region of high RTI activity between $z = -1.35$ Mm and $z = 0.65$ Mm. Height-averaged Fourier decomposition amplitudes are shown for out-of-plane magnetic field, B_y^2/μ_0, in-plane magnetic field, $(B_x^2 + B_z^2)/\mu_0$, total magnetic field, B^2/μ_0, and mass density of charges, ρ_c. The normalization value (E_0) used for magnetic field data is 10^{-3} J/m^3 and for ρ_c is 10^{-12} kg/m^3. The linear spectral fits $\langle A^n\rangle_z \propto n^\Lambda$ for (B^2/μ_0) and ρ_c are calculated using a subset of 11 mode amplitude values for $n = [5, 7, 10, 13, 18, 25, 35, 48, 66, 91, 126]$ that are approximately equidistributed over the range of the fit in the $\log_{10} n$ space, as illustrated with 'x' markers in the panel. Right: Time evolution of the spectral exponents Λ_B and Λ_{ρ_c} during the late non-linear and saturation phases of the RTI calculated at the same time instances as shown in the Fig. 3 snapshots. The errors of the fit are shown as vertical error bars.

of stable power spectra for structures in magnetic pressure and density of the charges (or electron density) in what may be analogous to the inertial range in turbulence. We further show that the power spectra for the two quantities are different, though interpretation of the specific power spectra obtained is beyond the scope of this paper and is subject for future work.

High resolution observations of prominences have been used to construct the power spectra of the structures over the regions with RTI dynamics (Hillier et al. 2017; Freed et al. 2016; Freed & McKenzie 2018), with the attention focused mostly on the velocity data. Assuming observed intensity to be a proxy for the plasma density, using different spectral lines for observations, e.g. neutral hydrogen H_α line or a line of an ionized element, e.g. CaIIH, one could also explore differences in density structure power spectra for plasma elements at different temperatures. As for the magnetic field power spectra, these require much more demanding spectropolarimetric observations and inversions. However, even maps of circular or linear polarisation spectra can be used as a proxy. Next generation of the 4-m class solar telescopes (DKIST, EST) should allow for such analysis in the future. It will allow for better understanding of the relationship between the electron density structure spectrum and the magnetic pressure structure spectrum, and may enable identification of the range and spectrum of magnetic structure scales present at solar prominence - corona interfaces.

Acknowledgements. This work was supported by the Spanish Ministry of Science through the project PGC2018-095832-B-I00 and the US National Science Foundation. The work was also supported by the FWO grant 1232122N. It contributes to the deliverable identified in FP7 European Research Council grant agreement ERC-2017-CoG771310-PI2FA for the project "Partial Ionization: Two-fluid Approach". The author(s) wish to acknowledge the contribution of Teide High-Performance Computing facilities to the results of this research. TeideHPC facilities are provided by the Instituto Tecnológico y de Energías Renovables (ITER, SA). URL: http://teidehpc.iter.es . Any opinion, findings, and conclusions or recommendations expressed in this material are those of the authors and do not necessarily reflect the views of the US National Science Foundation.

References

Berger, T., Hillier, A., & Liu, W. 2017, The Astrophysical Journal, 850, 60
Birn, J. & Hesse, M. 2007, Physics of Plasmas, 14, 082306
Chandrasekhar, S. 1961, Hydrodynamic and Hydromagnetic Stability, International series of monographs on physics (Clarendon Press)
Freed, M. S. & McKenzie, D. E. 2018, ApJ, 866, 29
Freed, M. S., McKenzie, D. E., Longcope, D. W., & Wilburn, M. 2016, ApJ, 818, 57
Hillier, A., Berger, T., Isobe, H., & Shibata, K. 2012a, ApJ, 746, 120
Hillier, A., Isobe, H., Shibata, K., & Berger, T. 2012b, ApJ, 756, 110
Hillier, A., Matsumoto, T., & Ichimoto, K. 2017, A&A, 597, A111
Hillier, A. & Polito, V. 2018, ApJ, 864, L10
Huba, J. D. 2007, NRL (Naval Research Laboratory) plasma formulary, revised

Jun, B.-I., Norman, M. L., & Stone, J. M. 1995, ApJ, 453, 332
Keppens, R., Xia, C., & Porth, O. 2015, ApJ, 806, L13
Labrosse, N., Heinzel, P., Vial, J. C., et al. 2010, Space Sci. Rev., 151, 243
Leake, J. E., Lukin, V. S., Linton, M. G., & Meier, E. T. 2012, ApJ, 760, 109
Ni, L. & Lukin, V. S. 2018, The Astrophysical Journal, 868, 144
Ni, L., Lukin, V. S., Murphy, N. A., & Lin, J. 2018a, ApJ, 852, 95
Ni, L., Lukin, V. S., Murphy, N. A., & Lin, J. 2018b, Physics of Plasmas, 25, 042903
Parchevsky, K. V. & Kosovichev, A. G. 2007, ApJ, 666, 547
Popescu Braileanu, B., Lukin, V. S., Khomenko, E., & de Vicente, Á. 2021a, A&A, 646, A93
Popescu Braileanu, B., Lukin, V. S., Khomenko, E., & de Vicente, Á. 2021b, A&A, 650, A181
Terradas, J., Soler, R., Luna, M., et al. 2016, ApJ, 820, 125
Zhou, Y., Williams, R. J., Ramaprabhu, P., et al. 2021, Physica D: Nonlinear Phenomena, 423, 132838

Appendix A: Evaluation of numerical dissipation

The simulations studied in this work were performed with idealized Ohm's law and strictly zero Ohmic diffusion coefficient. Likewise, the artificial analogues of the numerical magnetic diffusivity, viscosity and conductivity were all set to zero. The only stabilizing method employed was the filtering. Therefore, the filtering provides the numerical dissipation mechanism that allows for dissipation of the currents and magnetic reconnection in our model. In order to evaluate the amount of this numerical dissipation we consider the numerical details of how the filtering acts. The filter employed in MANCHA3D-2F is a sixth-order digital filter following Parchevsky & Kosovichev (2007). It is based on the filtering function $G(k\Delta x) = 1 - \sin^6\left(\frac{k\Delta x}{2}\right)$. The frequency of application of the filter in our simulation was every 5 time steps.

If one considers that the application of the filter at a given time step consists in changing a variable by

$$\frac{\partial u}{\partial t} = \frac{(u(x) - u_{\rm filt}(x))}{\Delta t} = \sum_{m=-3}^{3} d_{\rm m} u(x+m\Delta x)/\Delta t, \tag{A.1}$$

where u is a variable before filtering and $B_{\rm filt}$ is after filtering, and Δt is the time interval between two successive application of the filtering. The coefficients $d_{\rm m}$ take the values,

$$\begin{aligned} d_m &= [d_{-3}, d_{-2}, d_{-1}, d_0, d_1, d_2, d_3] \qquad (A.2)\\ &= [-1, 6, -15, 20, -15, 6, -1]/64. \end{aligned}$$

Since the filter is 6th order, it introduces a 6th order dissipation, which can be related to the time-change of u as,

$$\frac{\partial u}{\partial t} = \eta_6^F \Delta^6 u, \tag{A.3}$$

where η_6^F is the dissipation coefficient we are looking for. Assuming a discrete 2nd order 6th derivative of u on a symmetric stencil along the direction x,

$$\Delta^6 u = \frac{\partial^6 u}{\partial x^6} = \sum_{m=-3}^{3} c_{\rm m} u(x+m\Delta x)/\Delta x^6, \tag{A.4}$$

with $c_m = 64 d_m$, the coefficient η_6^F can now be evaluated as:

$$\eta_6^F = \frac{\Delta x^6}{64\Delta t}. \tag{A.5}$$

In this estimate, Δx is the size of our numerical grid. After introducing the values of Δx and Δt from simulations, the coefficient of the numerical dissipation obtained using Eq. (A.5) has the value $\eta_6^F = 4.714 \times 10^{18}$ m^6 s^{-1}.

In order to check the correctness of the above order of magnitude estimate and to get a better understanding of the numerical dissipation caused by the filtering we have computed η_6^F from the simulation data. For that, we have re-run the simulations for a short interval of time between 534.5 and 535.0 sec, applying the filtering either every 1, 5 or 20 time steps. Using these data, we made the linear regression between the corresponding terms in the induction equation, assuming 6th order dissipation,

$$y = \eta_6^F s + c, \tag{A.6}$$

where

$$\begin{aligned} s &= \Delta^6 \mathbf{B}; \qquad (A.7)\\ y &= \frac{\partial \mathbf{B}}{\partial t} - \nabla \times v \times \mathbf{B}. \end{aligned}$$

The regression was made separately for x and z components of $\mathbf{B}$, giving similar results for the η_6^F. The results of this calculation are shown in Figure A.1. The left panel of this figure demonstrates a well-defined linear dependence between $y = \partial\mathbf{B}/\partial t - \nabla \times v \times \mathbf{B}$ and $s = \Delta^6\mathbf{B}$, with a very narrow scatter of the data points, confirming that our numerical dissipation is well represented by the 6th order. The value of the dissipation coefficient, obtained after the linear fit to the data points, $\eta_6^F = 4.5 \times 10^{18}$ m^6 s^{-1}, coincides extremely well with the order of magnitude estimate given by the Eq. (A.5).

The right hand side panel of Figure A.1 shows how the value of η_6^F, obtained after fitting the numerical data, depends on the frequency of application of the filter (lines of different color) and on the mode number of the structures in the simulations. In order to obtain the dependence on the mode number, we applied a 2D high-pass Fourier filter to $y(x,z) = \partial\mathbf{B}/\partial t - \nabla \times v \times \mathbf{B}$ and $s(x,z) = \Delta^6\mathbf{B}$ variables calculated for a given snapshot, prior to computing the linear regression. We have retained all the modes with a mode number above a given value n, being n the mode number shown at the horizontal axis of the right hand side panel of Figure A.1. One can appreciate that the dependence of η_6^F on the mode number is rather weak, meaning that our numerical dissipation affects equally the scales up to $n = 300$, i.e. down to $L = 1/n \approx 6.8$ grid points. The values of η_6^F also scale well with the frequency of application of the filter. After we have re-scaled the curves for the different filtering frequency, the resulting values vary between 4×10^{18} and 5×10^{18} m^6 s^{-1}, which is, again, very close to our order of magnitude estimate from Eq. (A.5).

The effects of numerical diffusivity can be compared to the magnetic diffusivity due to physical Spitzer resistivity at a given spatial scale. For this

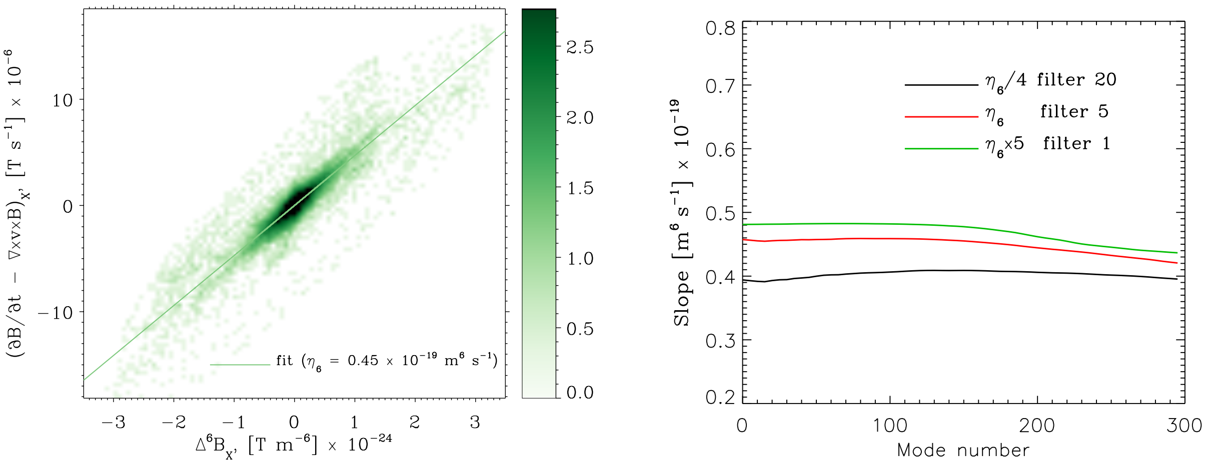

Fig. A.1. Left: Scatter plot showing the dependence between the terms of the induction equation, $y = \partial\mathbf{B}/\partial t - \nabla \times v \times \mathbf{B}$ (vertical axis) and $s = \Delta^6\mathbf{B}$ (horizontal axis). The intensity of the color indicated the number of spatial data points with the given values of (s, y) in $\log_{10}$ units. The green line shows the linear fit to the distribution, with the value of the slope η_6^F indicated in the figure. Right: dependence of the slope η_6^F on the spatial mode number, obtained after the fitting to the simulation data (as those from the left panel) for three simulations with the different values of the filtering frequency: every 1 time step (green line), every 5 time steps (red line), and every 20 time steps (black line). The dependence on the mode number is obtained after applying a 2D Fourier high-pass filter to $y = \partial\mathbf{B}/\partial t - \nabla \times v \times \mathbf{B}$ and $s = \Delta^6\mathbf{B}$ variables in each case.

purpose, we calculate the Spitzer resistivity as $\eta_{\parallel} = \eta_{\perp}/1.96$, with $\eta_{\perp}$ given in Huba (2007):

$$\eta_{\perp} = 1.03 \times 10^{-4} Z \ln(\Lambda) T_{\mathrm{eV}}^{-3/2}\,\Omega\,\mathrm{m}. \tag{A.8}$$

Here T_{eV} is the temperature in eV units, $Z = 1$ in our case, and we consider $\ln(\Lambda) = 10$. Using the temperature at the center of the current sheet $T = 2.2 \times 10^4$ K, we obtain the value of $\eta_{\parallel} = 2.01 \times 10^{-4}$ Ω m. Comparing the 6th order numerical diffusivity with the physical resistivity on the current sheet scale, we consider the length unit L as being the width of the current sheet measured from the simulation, i.e. $L = \lambda_J = 5.3$ km (see Fig. 5), and calculate $\eta_6^F \mu_0/L^4 = 7.51 \times 10^{-3} \Omega\,\mathrm{m} \gg \eta_{\parallel}$. We thus observe that the numerical dissipation on the current sheet scale is more than an order of magnitude greater than the expected physical dissipation, justifying the fact that the latter has been neglected in our simulation.